

## ANNEALING A FOLLOW-UP PROGRAM: IMPROVEMENT OF THE DARK ENERGY FIGURE OF MERIT FOR OPTICAL GALAXY CLUSTER SURVEYS

HAO-YI WU<sup>1</sup>, EDUARDO ROZO<sup>2,3,4</sup>, RISA H. WECHSLER<sup>1</sup>

*Received 2009 July 16; accepted 2010 March 8; published 2010 March 31*

### ABSTRACT

The precision of cosmological parameters derived from galaxy cluster surveys is limited by uncertainty in relating observable signals to cluster mass. We demonstrate that a small mass-calibration follow-up program can significantly reduce this uncertainty and improve parameter constraints, particularly when the follow-up targets are judiciously chosen. To this end, we apply a simulated annealing algorithm to maximize the dark energy information at fixed observational cost, and find that optimal follow-up strategies can reduce the observational cost required to achieve a specified precision by up to an order of magnitude. Considering clusters selected from optical imaging in the Dark Energy Survey, we find that approximately 200 low-redshift X-ray clusters or massive Sunyaev–Zel’dovich clusters can improve the dark energy figure of merit by 50%, provided that the follow-up mass measurements involve no systematic error. In practice, the actual improvement depends on (1) the uncertainty in the systematic error in follow-up mass measurements, which needs to be controlled at the 5% level to avoid severe degradation of the results; and (2) the scatter in the optical richness–mass distribution, which needs to be made as tight as possible to improve the efficacy of follow-up observations.

*Subject headings:* cosmological parameters — cosmology: theory — galaxies: clusters — galaxies: halos — methods: statistical

### 1. INTRODUCTION

The dynamical properties of dark energy can be constrained with two phenomena. The first is the expansion of the universe: dark energy has dominated the energy density of the universe for the past 4 billion years and has accelerated its expansion. The second is the growth of structure; since dark energy counteracts gravitational attraction, it slows the growth of structure. Galaxy cluster surveys explore both phenomena at the same time: the abundance and the correlation function of galaxy clusters depend on expansion history and structure growth, thus providing powerful probes of dark energy. Given the statistical power of ongoing and future surveys, galaxy clusters have become an indispensable probe of dark energy (e.g. Wang & Steinhardt 1998; Haiman et al. 2001; Holder et al. 2001; Levine et al. 2002; Hu 2003; Rozo et al. 2007a,b, 2010, and references therein).

Four cluster detection methods have been well established: the intracluster hot gas can be identified via X-ray (e.g., Ebeling et al. 1998, 2000, 2001; Vikhlinin et al. 1998; Böhringer et al. 2004) or Sunyaev–Zel’dovich (SZ) effects (e.g., Staniszewski et al. 2009; Hincks et al. 2009, see also Carlstrom et al. 2002); the mass concentrations can be identified using weak lensing shear (e.g., Wittman et al. 2001, 2006); or the galaxies in clusters can be identified in optical or infrared surveys (e.g., Postman et al. 1996; Koester et al. 2007; Eisenhardt et al. 2008). Large cluster surveys using each method are ongoing or forthcoming, and cosmological parameter constraints from cluster surveys have recently become competitive with other dark energy probes

(e.g., Mantz et al. 2008; Henry et al. 2009; Rozo et al. 2010; Vikhlinin et al. 2009b).

The key issue for extracting cosmological information from clusters is the fidelity of the mass tracer. In a survey, the mass tracer can be self-calibrated by combining the information from counts and sample variance (Lima & Hu 2004). In addition, if a sample or sub-sample of clusters is observed using multiple methods, the cluster mass can be further calibrated (e.g., Majumdar & Mohr 2003, 2004; Cunha 2009; Cunha et al. 2009). Determining the most effective approach to improve the constraining power of clusters using multiple mass tracers is particularly timely, as multi-wavelength observations will soon become available for large cluster samples.

In this work, we focus on follow-up observations for optical cluster surveys. We are particularly interested in how dark energy constraints from these surveys can be improved when a sub-sample of the clusters has better mass measurements from other methods, e.g., X-ray or SZ. Our goal is to characterize how follow-up observations should be designed and what precision is required in order to maximize dark energy information.

Optical surveys identify massive clusters as agglomerations of galaxies. Since the physics of galaxy formation is much more complicated than the physics of hot intracluster gas, optical mass tracers are not as well understood as X-ray or SZ mass tracers. Nevertheless, the optical richness–mass distribution can be empirically determined, and precise cosmological parameters have been derived from optically selected cluster samples (e.g., Gladders et al. 2007; Rozo et al. 2010). In the near future, optical surveys such as the Dark Energy Survey (DES<sup>5</sup>), the Panoramic Survey Telescope & Rapid Response System<sup>6</sup>, and the Large Synoptic Survey Telescope<sup>7</sup> will be able to identify substantially larger and higher-redshift cluster samples, which will significantly improve our knowl-

<sup>1</sup> Kavli Institute for Particle Astrophysics and Cosmology, Physics Department, and SLAC National Accelerator Laboratory, Stanford University, Stanford, CA 94305, USA; hywu@stanford.edu, rwechsler@stanford.edu

<sup>2</sup> The Center for Cosmology and Astro-Particle Physics, The Ohio State University, Columbus, OH 43210, USA

<sup>3</sup> The Kavli Institute for Cosmological Physics, Chicago, Illinois 60637, USA; erozo@kicp.uchicago.edu

<sup>4</sup> Einstein Fellow

<sup>5</sup> <http://www.darkenergysurvey.org>

<sup>6</sup> <http://pan-starrs.ifa.hawaii.edu>

<sup>7</sup> <http://www.lsst.org>

edge of dark energy equation of state  $w$ .

In this work, we assume the statistical power and parameters relevant to DES, apply the self-calibration method proposed by Lima & Hu (2004) to calculate our fiducial cosmological parameter constraints and explore how follow-up observations will improve dark energy constraints. Throughout, we quantify dark energy constraints with the figure of merit (FoM) proposed in the Report of the Dark Energy Task Force (Albrecht et al. 2006):

$$\text{FoM} = 1/\sqrt{\det \text{Cov}(w_0, w_a)} = [\sigma(w_a)\sigma(w_p)]^{-1}, \quad (1)$$

where  $w = w_0 + (1-a)w_a$  and  $w_p$  is calculated at the pivot redshift for which  $w$  is best constrained. The current value of the FoM from WMAP5, SNe, and BAO is 8.326 (Wang 2008). As a reference, the DETF report predicts that the FoM from Stage III cluster surveys (of which DES is an example) will range from 6.11 to 35.21, depending on the prior on the observable–mass distribution.

Assuming that the observable–mass distribution follows power laws in both mass and redshift, we find that the FoM expected from a DES-like survey is 15.5 using a self-calibrated analysis. We apply a simulated annealing algorithm to design follow-up strategies that maximize the FoM, starting with the limiting case in which follow-up mass measurements have infinite precision. We then study how the FoM improvements depend on real-world complications, finding that the efficacy of follow-up observations is likely to be limited by the systematic error in follow-up mass measurements. We finally consider observational issues and design different cost-effective follow-up strategies for X-ray and SZ.

Majumdar & Mohr (2003, 2004) have previously investigated how follow-up mass measurements of a fraction of the X-ray or SZ selected cluster sample can constrain the cluster evolution and improve dark energy constraints. Our major improvement upon these studies is the optimization of follow-up strategies. We also include counts-in-cells and mass binning, and explore how scatter and possible systematic error of mass tracers can affect the efficacy of follow-up observations.

Cunha (2009) has recently studied the joint analysis of overlapping optical and SZ cluster surveys. By studying the cluster abundances in both surveys, the observable–mass distribution can be cross-calibrated. In contrast to this study, we concentrate on one survey and its follow-up observations. That is, our method does not require another complete survey but instead focuses on a small and optimized follow-up program.

This paper is organized as follows. We briefly review dark energy constraints from clusters and the self-calibration analysis in Section 2.1 and describe our survey and model assumptions in Section 2.2. We present the modeling for follow-up observations in Section 3.1 and the optimization procedure in Section 3.2. Real-world complications of follow-up observations are explored in Section 4. Optimizations considering observational issues specific to X-ray and SZ clusters are carried out in Section 5. We discuss other relevant studies in Section 6 and conclude in Section 7.

## 2. DARK ENERGY CONSTRAINTS FROM GALAXY CLUSTERS

### 2.1. Self-calibration: A Review

In this section, we briefly review the self-calibration formalism developed by Lima & Hu (2004). For detailed discussions, we refer the reader to Lima & Hu (2004, 2005, 2007), Hu & Cohn (2006), and Wu et al. (2008).

In a galaxy cluster survey, one studies how cluster counts

depend on some cluster mass proxy to infer the dark matter halo mass function, which provides constraints on the properties of dark energy. To infer the mass function from data, one needs to relate the observable properties of clusters to the halo mass; thus, the uncertainty in this observable–mass distribution limits the constraining power of clusters. The observable–mass distribution can be self-calibrated using a counts-in-cells analysis, in which the survey volume is divided into small cells and the halo bias can be calculated from the sample variance among the cells. By measuring both counts and sample variance, the mass function and the halo bias are fit simultaneously, the observable–mass distribution can be self-calibrated, and the dark energy constraints can be improved.

Let us consider a cell of volume  $V_c$  in a narrow redshift range in a survey. We denote the cluster mass proxy by  $M_{\text{obs}}$  and further bin our cluster sample in  $M_{\text{obs}}$  with a binning function  $\phi(\ln M_{\text{obs}})$ , which equals unity inside the bin and zero elsewhere. In this bin, the mean cluster counts ( $\bar{m}$ ) and the mean cluster bias ( $\bar{b}$ ) can be calculated from the mass function  $dn/d \ln M$ , the halo bias  $b(M)$ , and the observable–mass distribution  $P(\ln M_{\text{obs}} | \ln M)$ :

$$\bar{m} = V_c \int d \ln M \frac{dn}{d \ln M} \langle \phi | \ln M \rangle, \quad (2)$$

$$\bar{b} = \frac{V_c}{\bar{m}} \int d \ln M \frac{dn}{d \ln M} b(M) \langle \phi | \ln M \rangle, \quad (3)$$

where

$$\langle \phi | \ln M \rangle = \int d \ln M_{\text{obs}} P(\ln M_{\text{obs}} | \ln M) \phi(\ln M_{\text{obs}}). \quad (4)$$

We assume the redshift bin is thin enough and simply use the function values at the middle redshift instead of averaging over the redshift bin.

The mean cluster bias  $\bar{b}$  determines the number fluctuations among cells due to the large-scale clustering. If cell  $i$  has cluster counts  $m_i$  and bias  $b_i$ , the corresponding sample variance among the cells is given by

$$S_{ij} = \langle (m_i - \bar{m}_i)(m_j - \bar{m}_j) \rangle = \bar{m}_i \bar{m}_j \bar{b}_i \bar{b}_j \sigma_{V_c}^2, \quad (5)$$

where  $\sigma_{V_c}^2$  is the variance of the dark matter density fluctuation in volume  $V_c$ . We assume that the cell volume is large enough for the covariance between cells to be negligible.

In a survey, one observes  $\bar{m}_i$  and  $S_{ij}$ , calculates  $\bar{b}_i$ , and self-calibrates  $P(\ln M_{\text{obs}} | \ln M)$  based on Equations 2 and 3. We use matrix notations  $\bar{\mathbf{m}}$  and  $\mathbf{S}$  to indicate the data in multiple mass and redshift bins and further define  $\mathbf{C} = \text{diag}(\bar{\mathbf{m}}) + \mathbf{S}$ . The constraints on model parameters can be obtained from the Fisher matrix

$$F_{\alpha\beta} = \bar{\mathbf{m}}_{,\alpha}^T \mathbf{C}^{-1} \bar{\mathbf{m}}_{,\beta} + \frac{1}{2} \text{Tr}[\mathbf{C}^{-1} \mathbf{S}_{,\alpha} \mathbf{C}^{-1} \mathbf{S}_{,\beta}], \quad (6)$$

where the comma followed by a subscript indicates the partial derivative with respect to a model parameter, and the derivatives are with respect to cosmological parameters and the parameters characterizing the observable–mass distribution. We invert this Fisher matrix to obtain the covariance matrix and constraints on model parameters.

The second term in this Fisher matrix characterizes the information from the sample variance. Since the sample variance depends on both cosmology and observable–mass distri-

bution, this “noise” in cluster counts actually provides “signal.” As we will see in Section 3.1, an analogous Fisher matrix is used to calculate the constraints from follow-up observations. In those observations, the variance in follow-up mass measurements will provide critical information for breaking the degeneracies between model parameters.

## 2.2. Survey and Model Assumptions

In this work, we consider a DES-like optical survey with a survey area of  $5000 \text{ deg}^2$ , and a survey depth such that clusters with redshift  $z < 1$  are robustly identified. For the counts-in-cells analysis, the survey volume is divided into cells of area =  $10 \text{ deg}^2$  and  $\Delta z = 0.1$  (see, e.g., Lima & Hu 2004). We assume that the mass threshold for the survey is  $M_{\text{obs}} = 10^{13.7} h^{-1} M_{\odot}$ , and that the cluster sample is binned by  $M_{\text{obs}}$  into eight bins with logarithmic bin size  $\Delta \log_{10} M_{\text{obs}} = 0.2$ . Note that the mass threshold and binning are based on the mass proxy  $M_{\text{obs}}$  rather than the true cluster mass  $M$ . We have tested the impact of the binning on our results and found that this binning is fine enough that we do not lose information from the data. Finer binning is also unnecessary because the scatter between the observable and mass sets an effective mass resolution.

For the observable–mass distribution  $P(\ln M_{\text{obs}} | \ln M)$ , we assume a Gaussian distribution with mean  $(\ln M + \ln M_{\text{bias}})$  and variance  $\sigma_{\text{obs}}^2$ . Both  $\ln M_{\text{bias}}$  and  $\sigma_{\text{obs}}^2$  are assumed to vary linearly with  $\ln M$  and  $\ln(1+z)$  via

$$\ln M_{\text{bias}} = \ln M_0 + \alpha_M \ln(M/M_{\text{pivot}}) + \alpha_z \ln(1+z) \quad (7)$$

$$\sigma_{\text{obs}}^2 = \sigma_0^2 + \beta_M \ln(M/M_{\text{pivot}}) + \beta_z \ln(1+z), \quad (8)$$

giving nuisance parameters:  $(\ln M_0, \alpha_M, \alpha_z, \sigma_0^2, \beta_M, \beta_z)$ . For our fiducial model, we assume an unbiased and non-evolving observable–mass distribution with  $\sigma_0 = 0.5$  (all other parameters are set to zero), which is consistent with the results in Gladders et al. (2007) and Rozo et al. (2010). In addition,  $M_{\text{pivot}}$  should be close to the mass scales of interest; we choose  $M_{\text{pivot}} = 10^{13.7} h^{-1} M_{\odot}$ , noting that the precise value of  $M_{\text{pivot}}$  does not affect our results.

Throughout this work, we assume the *Wilkinson Microwave Anisotropy Probe Five Year (WMAP5)* cosmological parameters (Komatsu et al. 2009;  $w_0 = -1$ ,  $w_a = 0$ ,  $\Omega_{\text{DE}} = 0.726$ ,  $\Omega_k = 0$ ,  $\Omega_m h^2 = 0.136$ ,  $\Omega_b h^2 = 0.0227$ ,  $n_s = 0.960$ ,  $\Delta_{\zeta} = 4.54 \times 10^{-5}$  at  $k = 0.05 \text{ Mpc}^{-1}$ ), and use the Planck-prior Fisher matrix provided by W. Hu and Z. Ma. We use the linear matter power spectrum calculated by CAMB (Lewis et al. 2000). The halo mass is defined with spherical overdensity of  $\Delta = 200$  with respect to the mean matter density, and we use the updated mass function from Tinker et al. (2008) and the halo bias function from Sheth et al. (2001)<sup>8</sup>. Under these assumptions, we expect that a DES-like survey will observe approximately  $2 \times 10^5$  clusters in total.

## 3. IMPROVING DARK ENERGY CONSTRAINTS WITH OPTIMAL FOLLOW-UP STRATEGIES

### 3.1. Constraints from Follow-up Mass Measurements

In this section, we calculate the additional constraints from follow-up observations. Given the optical cluster sample from

<sup>8</sup> An updated halo bias function is available in Tinker et al. (2010); the difference between the two functions does not significantly affect our results. We also note that the mass function and the halo bias function we use are not in a consistent framework; since we only use their dependence on cosmology, this inconsistency is not important.

a DES-like survey, we select some clusters from each mass and redshift bin to follow up—for example, to measure their properties in X-ray or SZ—and estimate the cluster mass more precisely. These follow-up mass measurements provide further constraints on the observable–mass distribution, thus improving the dark energy constraints of the original survey. Throughout Section 3, we assume the follow-up observations provide mass measurements with infinite precision; the complications of follow-up mass tracers will be explored in Section 4.

Our goal is to constrain the scaling relation and the scatter of optical richness. We note that the term “scatter” usually has different meanings in theoretical and observational contexts. In the theoretical model, the scatter of  $\ln M_{\text{obs}}$  at fixed  $\ln M$  ( $\sigma_{\text{obs}}$  in our notation) is used because the model is based on the mass function, which is a function of  $M$ . In contrast, one observationally constrains the scatter of  $\ln M$  at fixed  $\ln M_{\text{obs}}$  because follow-ups are selected based on their  $M_{\text{obs}}$  (e.g., Rozo et al. 2009b). In general, the theoretical model is based on  $P(\ln M_{\text{obs}} | \ln M)$ , while observations put constraints on  $P(\ln M | \ln M_{\text{obs}})$ . Our goal is therefore to convert constraints on the latter distribution to constraints on the former.

Let us return to the original survey, focusing on the follow-up observations in a bin specified by  $\phi(\ln M_{\text{obs}})$  in a narrow redshift range. If the follow-up mass  $M_f$  perfectly recovers the true mass, the mean and variance of  $\ln M_f$  will read

$$\begin{aligned} \langle \ln M_f \rangle &= E[\ln M_f | \phi(\ln M_{\text{obs}})] \\ &\propto \int d \ln M \ln M \frac{dn}{d \ln M} \langle \phi | \ln M \rangle, \end{aligned} \quad (9)$$

and

$$\begin{aligned} V &= \text{Var}[\ln M_f | \phi(\ln M_{\text{obs}})] \\ &\propto \int d \ln M (\ln M - \langle \ln M_f \rangle)^2 \frac{dn}{d \ln M} \langle \phi | \ln M \rangle. \end{aligned} \quad (10)$$

The information from a single follow-up mass measurement is given by an analog of Equation 6:

$$\tilde{F}_{\alpha\beta}^{(i)} = \langle \ln M_f \rangle_{,\alpha} V^{-1} (\ln M_f)_{,\beta} + \frac{1}{2} V^{-1} V_{,\alpha} V^{-1} V_{,\beta}, \quad (11)$$

where the superscript ( $i$ ) indicates the mass and redshift bin from which we select follow-ups. If we follow up  $N_i$  clusters in bin  $i$ , the Fisher matrix for the whole follow-up program reads

$$\tilde{F}_{\alpha\beta} = \sum_i N_i \tilde{F}_{\alpha\beta}^{(i)}. \quad (12)$$

This Fisher matrix is added to the Fisher matrix of counts-in-cells (Equation 6) to improve the constraints on nuisance parameters<sup>9</sup>. Note that the second term in Equation 11 plays the role of “noise as signal” as in the case of counts-in-cells, characterizing the information included in the mass variance of follow-ups.

Figure 1 shows how follow-up observations improve the dark energy FoM (defined in Section 1). We calculate the ratio

<sup>9</sup> *Technical note.* In principle, when we calculate the Fisher matrix  $\tilde{F}_{\alpha\beta}$ , the derivatives should include cosmological parameters. However, to correctly model the cosmological information in follow-up observations, we need to include the covariance between the follow-up observations and the original cluster survey. For simplicity, we ignore this covariance and only consider the information for nuisance parameters, noting that the cosmological information is negligible for up to 1000 follow-ups.

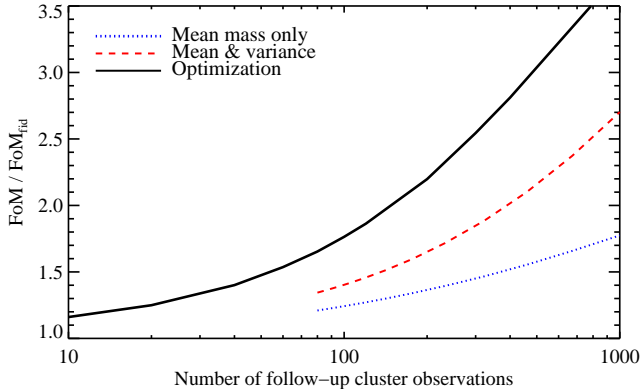


FIG. 1.— Improvement in the dark energy FoM due to follow-up observations, relative to the fiducial value ( $\text{FoM}_{\text{fid}}$ ) for a DES-like survey. The black solid curve corresponds to optimal follow-up strategies that maximize the FoM; the red dashed curve assumes that the follow-ups are evenly selected from all mass and redshift bins; the blue dotted curve also assumes even selection, ignoring the variance of the follow-up mass measurements. The follow-ups can significantly improve the FoM, especially when the target selection is optimized and when the variance of follow-up mass measurements is included.

between the improved FoM and the fiducial FoM from a DES-like survey (without follow-ups) and demonstrate how this ratio improves as the number of follow-up mass measurements increases. For the two lower curves, we assume that follow-up targets are evenly selected across all bins (i.e.,  $N_i = N_f/80$ , including eight bins in  $M_{\text{obs}}$  and ten bins in redshift). We also limit the number of follow-ups in each bin by the number of clusters that a DES-like survey is expected to observe.

The red dashed curve shows the improvement of the FoM using the information from both the mean and the variance of follow-up mass measurements (i.e., both terms in Equation 11). As can be seen, the follow-ups can substantially improve the FoM; for example, for 100 follow-up mass measurements, the FoM can be improved by 40.3%. For comparison, the blue dotted curve shows the improvement in the FoM using the information only from the mean of follow-up mass measurements (i.e., only the first term in Equation 11). As can be seen, lacking the information from the variance can substantially reduce the effectiveness of follow-ups. This case may be relevant to stacked cluster samples which provide the mean but not the variance of cluster mass. Finally, the black solid curve corresponding to the most significant improvement is based on the optimal follow-up strategies, which will be discussed in the next section.

In addition to evenly selected follow-up targets, we also investigate the case of selecting a fixed fraction of the cluster sample in each bin, which is assumed in Majumdar & Mohr (2003). This selection gives slightly lower FoM values than our evenly selected follow-ups; the reason will become clear in the next section.

### 3.2. Optimizing Follow-up Strategies: A Simulated Annealing Approach

Instead of selecting the same number of follow-up targets in all bins, in this section, we explore how we can further improve the FoM by optimally selecting the follow-ups. We pose the following optimization problem: for a fixed number of follow-up measurements,  $N_f$ , how should we select follow-up targets to maximize the FoM?

We use a slight variant of the Metropolis-based simulated annealing algorithm to find the optimal follow-up strategy.

The idea of simulated annealing comes from a physical phenomenon: when a metal cools slowly, its atoms will rearrange to achieve the minimum of internal energy. This rearrangement sometimes moves toward higher-energy states due to thermal fluctuations, which allow the system to overcome energy barriers separating different local minima. As the system cools, these thermal fluctuations become rare; provided the cooling process is slow enough, the system will eventually approach its global energy minimum.

The simulated annealing algorithm is suitable for our problem because our problem is combinatorial and the total number of configurations is factorially large. (If we use 80 bins, there are  $10^{52}$  configurations for  $N_f = 100$  and  $10^{121}$  configurations for  $N_f = 1000$ .) Following the guidelines in Press et al. (2002), we design our algorithm as follows:

1. The system configuration is characterized by the number of follow-up targets in each mass and redshift bin,  $\mathbf{N} = (N_1, \dots, N_{80})$ . (We use eight bins in  $M_{\text{obs}}$  and ten bins in redshift.) We note that the general configurations do not change with the detail of binning.
2. The rearrangement of clusters in bins, or the transition from one configuration to another, is designed as follows: given an initial configuration, for each “donor” bin  $i$ , we randomly pick a “receiver” bin  $j$  and transfer  $n_{\text{trans}}$  clusters to the receiver bin. Here  $j$  is randomly chosen from all available bins, and  $n_{\text{trans}}$  is a random integer between 0 and  $n_{\text{limit}}$ . We choose  $n_{\text{limit}}$  to be 1% of the total number of follow-ups  $N_f$ ; for example, if  $N_f = 100$ , we transfer 0 or 1 cluster at a time. We also require the number of follow-ups in each bin to be between zero and the number of clusters expected to be observed in that bin. After running  $i$  through all bins, i.e., letting each bin play the role of donor once, we reach a new nearby configuration.
3. The objective function is the FoM, which we are trying to maximize by sampling different configurations. Applying the idea of the Metropolis algorithm, we start from the current configuration ( $\mathbf{N}_i$ , with the FoM value  $F_i$ ) and sample a nearby configuration ( $\mathbf{N}_{\text{try}}$ , with the FoM value  $F_{\text{try}}$ ). If  $F_{\text{try}} > F_i$ ,  $\mathbf{N}_{\text{try}}$  is accepted at this step; that is, we set  $\mathbf{N}_{i+1} = \mathbf{N}_{\text{try}}$ . If  $F_{\text{try}} < F_i$ ,  $\mathbf{N}_{\text{try}}$  is accepted with probability  $\exp[(F_{\text{try}} - F_i)/T]$ . Here  $T$  is the “temperature” parameter that determines the probability of moving to a smaller FoM value (analogous to thermal fluctuations).
4. To design our annealing schedule, we start with a  $T$  value that roughly gives an acceptance rate of 0.2; this rate empirically indicates a fair sampling of the configuration space (see, e.g., Dunkley et al. 2005 for the case of Markov chain Monte Carlo). After running  $10^4$  iterations with this temperature, we lower the temperature by 10% and run 4000 iterations as one step of the annealing. We repeat this annealing procedure between 10 and 40 times (depending on the size of the configuration space) until the improvement in the FoM is negligible and the system “entropy” is low in the sense that clusters are concentrated in a few bins.

Since our configuration space is factorially large, we reduce its size to facilitate the sampling. We start with only 40 bins

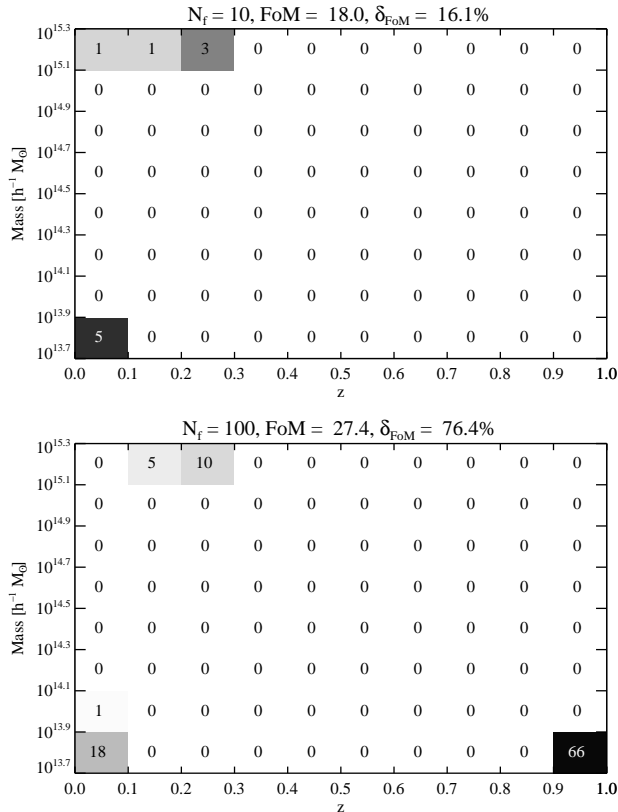


FIG. 2.— Optimal follow-up strategies that maximize the FoM at a given number of follow-up observations  $N_f$ , calculated with a simulated annealing algorithm. Each pixel corresponds to one mass and redshift bin in the optical cluster survey, and the corresponding number of follow-ups in this bin is shown. *Upper*:  $N_f = 10$ ; *lower*:  $N_f = 100$ . As can be seen, low-redshift bins are highlighted because they provide complementary information to the CMB prior. In addition, the follow-up strategies prefer the corners, because these bins provide the longest lever arms for constraining the mass and redshift dependence of the observable–mass distribution.

by doubling the bin size in  $M_{\text{obs}}$  and determine where the relevant bins are. We then return to our original binning and exclude irrelevant bins to reduce the size of the configuration space.

Regarding the convergence of our algorithm, we note that although the simulated annealing algorithm will eventually converge to the global optimum, pursuing this convergence is impractical due to the extremely large configuration space. We use a sufficiently high temperature at the beginning to ensure that the configuration space is fairly sampled, but we cannot guarantee that the global optimum is found at the end. However, after testing several different initial configurations, we find that various local optima are very close to each other. Each of these optima provides significant improvement when compared to the evenly selected follow-ups. We thus expect that our method provides a good solution to the optimization problem.

Figure 2 illustrates two examples of our optimization; the upper panel corresponds to ten follow-ups in total,  $N_f = 10$ , and the lower panel corresponds to  $N_f = 100$ . For  $N_f = 10$ , the optimal configuration focuses on the highest and the lowest mass bins at low redshift. This configuration reflects the fact that given the tight CMB prior, most of the constraining power of a cluster survey lies in the low-redshift cluster sample, which provides the longest possible lever arm for constraining the evolution in dark energy. This optimal follow-up strategy improves the FoM by 16.1% relative to the fiducial FoM of the survey. For  $N_f = 100$ , high-redshift clusters start to become important, and the improvement in the FoM is 76.4%, compared to 40.3% for uniform sampling. We note that in the highest-mass and lowest-redshift bins, clusters are very rare and we reach the limit of following up all clusters in these bins.

We can see that the optimal follow-up strategies always select clusters in the most extreme bins—only the corners of the mass and redshift bins shown in Figure 2 are populated. This result reflects our assumption that the observable–mass distribution depends on mass and redshift via power laws, which are well constrained by the extremes. These strategies also imply that following up a random fraction of the cluster catalog is inefficient as a way to improve the FoM, since typical clusters are in the low-mass and mid-to-high redshift regime.

In practice, following up clusters in the highest-redshift and lowest-mass bin is impractical, if not impossible. Consequently, we explore how superior this bin is relative to its neighbors. We find that this bin is not significantly better than other high-redshift and low-mass bins. The lowest-redshift bins, on the other hand, are always the most essential to follow up. Thus, for designing a practical follow-up program, one should always prioritize the lowest-redshift bins and try to extend to the high-redshift and low-mass regime. We will further explore the detectability and observational cost issues to find the most cost-effective strategies in Section 5.

The improvement in the FoM due to the optimization is shown as a black solid curve in Figure 1. We select various  $N_f$  values and apply the optimization algorithm to maximize the FoM. Compared to the case of uniformly sampled follow-ups, the optimization can further improve the FoM.

For an interesting comparison, we note that Frieman et al. (2003) optimized the supernova survey strategy to minimize the errorbar on  $w$ . They demonstrated different survey strategies to complement different CMB priors. We also note that Parkinson et al. (2007, 2010) applied simulated annealing to the design of baryon acoustic oscillation surveys.

#### 4. REQUIREMENTS FOR THE FOLLOW-UP MASS PROXY

##### 4.1. Scatter and Covariance of the Mass Proxies

So far we have assumed that follow-up observations can recover the true mass precisely; i.e.,  $M_f = M$ . In reality,  $M_f$  itself is a mass proxy and has a scatter  $\sigma_f$  around the true mass  $M$ . Moreover, this scatter may correlate with  $\sigma_{\text{obs}}$ , the scatter of  $M_{\text{obs}}$  around  $M$ . Therefore, a proper analysis of the effects of follow-up observations should include the observable–follow-up–mass distribution  $P(\ln M_{\text{obs}}, \ln M_f | \ln M)$ .

We assume that the follow-up mass tracer correlates with the true mass more tightly than the survey mass tracer does; for example, X-ray and SZ mass proxies have lower scatter than any known optical mass proxy (e.g., Kravtsov et al. 2006). We have assumed  $\sigma_{\text{obs}} = 0.5$  throughout our analysis; we further assume that  $\sigma_f = 0.1$  and that the two mass proxies,

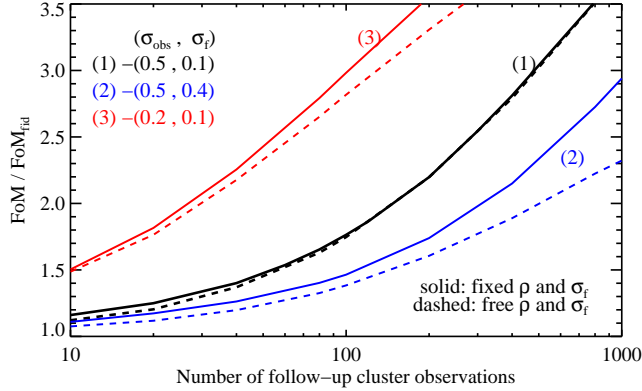


FIG. 3.— Impact of the scatter and the correlation of mass proxies on the effectiveness of optimized follow-up observations. Here we compare three sets of assumptions about  $\sigma_{\text{obs}}$  and  $\sigma_f$ ; for each set we show the cases of fixed (solid curves) and marginalized (dashed curves)  $\rho$  and  $\sigma_f$ . When  $\sigma_f \ll \sigma_{\text{obs}}$ , the FoM is almost unaffected by marginalization, as shown in (1). When  $\sigma_f$  is large, the effectiveness of follow-ups is degraded, as shown in (2). On the other hand, when the survey has small scatter (small  $\sigma_{\text{obs}}$ ), follow-ups can significantly improve the FoM, as shown in (3).

$\ln M_{\text{obs}}$  and  $\ln M_f$ , have a correlation coefficient  $\rho$ . No prior knowledge is assumed about  $\rho$ .

Let us assume that the observable–follow-up–mass distribution  $P(\ln M_{\text{obs}}, \ln M_f | \ln M)$  is a bivariate Gaussian distribution in  $(\ln M_{\text{obs}} - \ln M)$  and  $(\ln M_f - \ln M)$  with the covariance matrix

$$\begin{pmatrix} \sigma_{\text{obs}}^2 & \rho \sigma_{\text{obs}} \sigma_f \\ \rho \sigma_{\text{obs}} \sigma_f & \sigma_f^2 \end{pmatrix}.$$

The mean of  $\ln M_f$  is given by

$$E[\ln M_f | \phi(\ln M_{\text{obs}})] \propto \int d \ln M \frac{dn}{d \ln M} \int d \ln M_f \ln M_f \int \ln M_{\text{obs}} \phi(\ln M_{\text{obs}}) P(\ln M_{\text{obs}}, \ln M_f | \ln M). \quad (13)$$

The variance of  $\ln M_f$  can be calculated similarly. Since this variance involves both  $\sigma_{\text{obs}}$  and  $\sigma_f$ , in the limit  $\sigma_f^2 \ll \sigma_{\text{obs}}^2$ , we expect the variance of  $\ln M_f$  to be dominated by  $\sigma_{\text{obs}}^2$ . On the other hand, if  $\sigma_f$  is larger (i.e., the follow-up mass measurements have larger intrinsic scatter), the resulting mass variance of follow-ups will be larger and the FoM improvement will be less significant.

We find that different values of  $\rho$  barely affect the resulting FoM: positive  $\rho$  slightly improves the FoM, while negative  $\rho$  slightly degrades the FoM. When compared to positive  $\rho$ , negative  $\rho$  widens the mass range of the follow-ups (with larger variance in  $\ln M_f$ ) and has slightly less constraining power. The reason is that when the correlation is negative,  $\sigma_{\text{obs}}$  and  $\sigma_f$  tend to scatter  $M_{\text{obs}}$  and  $M_f$  to opposite directions, and cluster samples selected based on  $M_{\text{obs}}$  will have larger variance in  $M_f$ . Since the differences are small, we only show the case of a zero correlation for demonstration.

We allow the scatter  $\sigma_f$  and the correlation coefficient  $\rho$  to be additional free parameters in the Fisher matrix (Equation 12) and study their impact. In Figure 3, we explore how different assumptions of scatter affect the FoM improvement (based on the optimal configurations found in Section 3.2). Each pair of solid and dashed curves corresponds to a set of assumptions about  $\sigma_{\text{obs}}$  and  $\sigma_f$ ; the solid curve corresponds to fixed  $\sigma_f$  and  $\rho$  in the Fisher matrix, while the dashed curve corresponds to marginalized  $\sigma_f$  (with a prior of 0.05 on  $\sigma_f^2$ )

and  $\rho$  (with no prior).

The two black curves in the middle, labeled as (1), correspond to our baseline assumption about the scatter:  $\sigma_{\text{obs}} = 0.5$  and  $\sigma_f = 0.1$ . As can be seen, the uncertainty in  $\rho$  barely degrades the FoM. This minor effect is due to the small  $\sigma_f$ ; given such a small scatter, the follow-up mass will closely follow the real mass even for an uncertain correlation.

On the other hand, if  $\sigma_f$  is large, the follow-ups have large intrinsic scatter and provide less constraining power. We demonstrate the degradation with the two blue curves at the bottom, labeled as (2), which correspond to a high scatter in follow-ups:  $\sigma_f = 0.4$ . Comparing the blue solid curve to the black solid curve, we can see that the FoM is degraded due to the larger scatter in follow-ups. If we further consider the uncertainty in  $\rho$ , the blue dashed curve shows stronger degradation than the baseline case.

We also explore the effect of  $\sigma_{\text{obs}}$ . The two red curves at the top, labeled as (3), correspond to the case of a low scatter in  $\ln M_{\text{obs}}$ :  $\sigma_{\text{obs}} = 0.2$ . Comparing the red solid curve to the black solid curve, we can see that the FoM is significantly improved due to the smaller mass variance of the follow-ups. Since the follow-ups are selected by  $M_{\text{obs}}$ , lowering  $\sigma_{\text{obs}}$  leads to follow-ups with a less spread in mass and provides better constraints. The red dashed curve shows that marginalizing over  $\sigma_f$  and  $\rho$  only modestly degrades this result, since in this regime both mass tracers have very high fidelity.

We note that the FoM improvement due to a small  $\sigma_{\text{obs}}$  comes from the follow-ups rather than self-calibration. When we lower  $\sigma_{\text{obs}}$  from 0.5 to 0.2, the fiducial FoM from self-calibration (without follow-ups) barely changes. This result reflects the fact that simply reducing the value of the scatter is not as effective as improving the constraints on the scatter.

We also note that  $\sigma_f$  and  $\rho$  are assumed to be independent of mass and redshift; detailed properties of  $\sigma_f$  and  $\rho$  are beyond the scope of this work. However, possible dependence of these parameters on mass and redshift, if not well constrained, may severely degrade the FoM (see, e.g., Sahlén et al. 2009).

In summary, we have found that as long as  $\sigma_f$  is sufficiently small, the effects of  $\sigma_f$  and  $\rho$  are negligible, and the uncertainty in  $\rho$  has only a modest impact on the efficacy of the follow-up observations.

#### 4.2. Systematic Error in Follow-up Mass Measurements

In this section, we ignore the scatter in the follow-ups and focus on the possibility that follow-up mass measurements systematically deviate from the true mass by a constant factor  $d$ . The mean of  $\ln M_f$  takes the form

$$E[\ln M_f | \phi(M_{\text{obs}})] = \ln d + E[\ln M | \phi(M_{\text{obs}})]. \quad (14)$$

The parameter  $d$  characterizes the average systematic error of the follow-up mass measurements and has no impact on the variance of  $\ln M_f$ . We include  $\ln d$  as an additional nuisance parameter in the Fisher matrix (Equation 12) and study its impact on the FoM. We are looking for the required constraints on  $\ln d$  to avoid severe degradation of the FoM.

When comparing Equations 7 and 14, we note that  $\ln M_{\text{bias}}$  and  $\ln d$  are completely degenerate in determining  $E[\ln M_f | \phi]$ . On the other hand, since  $\ln d$  does not affect the variance of  $\ln M_f$  in a bin (Equation 10), this variance can provide information for  $\ln M_{\text{bias}}$  and break the degeneracy. Here we demonstrate again the importance of the mass variance in follow-up observations.

Figure 4 shows how the systematic error degrades the efficacy of our optimal follow-up strategies. We set the fidu-

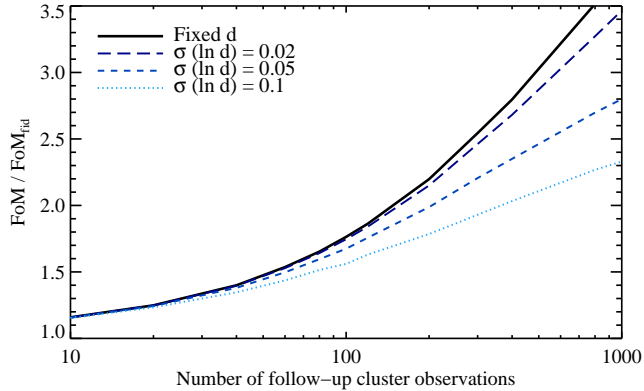


FIG. 4.— Impact of systematic error in follow-up mass measurements on our optimal follow-up results. We assume that the follow-up mass measurements systematically deviate from the true mass by a constant factor  $d$  and compare different prior constraints on  $\ln d$ . Uncertainty in  $d$  can substantially degrade the efficacy of follow-ups; for about 200 follow-ups, a degradation of less than 10% requires  $\sigma(\ln d) < 0.05$ .

cial value of  $\ln d$  to be 0 and compare different prior constraints on  $\ln d$ . As can be seen, for approximately 200 follow-ups, a degradation of less than 10% in the FoM requires  $\sigma_{\text{prior}}(\ln d) < 0.05$ . The required prior constraint on  $\ln d$  depends on the number of follow-up observations; larger follow-up programs require even higher precision. Consequently, it is very likely that the systematic error in mass measurements will determine the efficacy of follow-up observations.

#### 5. OPTIMIZING X-RAY AND SZ FOLLOW-UP PROGRAMS: OBSERVATIONAL ISSUES

In previous sections, we assumed that all optically selected clusters have an equal chance to be followed up, regardless of their mass and redshift. In reality, observing optically selected low-mass or high-redshift clusters may be very difficult or even impossible with some methods; the optimization in Section 3.2 is thus impractical. For example, observing high-redshift clusters in X-ray requires substantially (if not prohibitively) more telescope time and sometimes has limited improvement in parameter constraints. Thus, we would like to optimize the follow-up strategy considering both the FoM and the cost of telescope time. In this section, instead of assuming a fixed number of follow-ups, we study how to optimize the follow-up strategy with limited observational cost. We first model the observational cost in Section 5.1 and then demonstrate the optimization in Section 5.2.

##### 5.1. Observability and Cost Proxies

For X-ray, we expect that a precise mass measurement requires certain photon counts; therefore, we assume that the telescope time for observing a cluster is inversely proportional to its flux of X-ray photons. This flux is proportional to  $L_X/D_L^2$ , where  $L_X$  is the X-ray luminosity and  $D_L(z)$  is the luminosity distance. We assume a self-similar scaling relation from the fit of Vikhlinin et al. (2009a),  $L_X \propto M_{500c}^{1.6} E^{1.85}(z)$ . This fit is based on the mass with overdensity 500 times the critical density ( $M_{500c}$ ), while we calculate the mass function using overdensity 200 times the mean matter density ( $M_{200m}$ ); therefore, we convert  $M_{500c}$  to  $M_{200m}$  using the fitting formula in Hu & Kravtsov (2003). We normalize the observational cost such that one unit corresponds to the telescope time for observing a cluster of mass  $10^{15.1} h^{-1} M_\odot$  at redshift 0.05. Measuring the mass of such a cluster to 10% accuracy using

$Y_X$  takes approximately 0.13 ks with a single XMM MOS camera (A. Mantz 2009, private communication)<sup>10</sup>. We note that we use  $\sigma_f = 0.1$  for X-ray clusters (e.g., Kravtsov et al. 2006).

For SZ, we expect that the observational time is proportional to the inverse square of signal-to-noise ratio,  $S/N \propto Y/\sqrt{\Omega}$ , where  $Y$  is the integrated Compton- $y$  parameter and  $\Omega$  is the angular size of the cluster. In virial equilibrium,  $Y \propto M^{5/3} \rho_m^{1/3}/D_A^2$ , where  $\rho_m(z)$  is the mean matter density and  $D_A(z)$  is the angular diameter distance. The dependence on angular size comes from averaging the total cluster emission over some number of detectors. The SZ cost proxy is therefore proportional to  $D_A^2 M_{200m}^{-8/3} (1+z)^{-4}$ . In addition, we exclude clusters of redshift less than 0.1; these clusters have large angular sizes and are contaminated by the primary CMB anisotropy. We also exclude clusters of mass less than  $10^{14.1} h^{-1} M_\odot$  because they are subject to significant background confusion (Holder et al. 2007). We normalize the observational cost such that one unit corresponds to the telescope time for observing a cluster of mass  $10^{15.1} h^{-1} M_\odot$  at redshift 0.15. To observe such a cluster, it takes about 30 minutes to obtain  $S/N=10$  with the South Pole Telescope (SPT) (D. Marrone & B. Benson 2009, private communication). We use a slightly larger scatter for SZ clusters,  $\sigma_f = 0.2$ ; simulations have suggested that this scatter may be intrinsic (e.g., Shaw et al. 2008), and projection effects can further increase the scatter. Note that we only consider intrinsic scatter and ignore systematic errors in the mass measurements from both X-ray and SZ clusters.

The top panels in Figure 5 present the mass and redshift dependence of the cost proxies. As can be seen, X-ray and SZ cost proxies have different patterns. The cost of X-ray clusters increases rapidly with redshift, while the cost of SZ clusters is almost constant with redshift. The latter is primarily sensitive to mass rather than redshift; thus, for SZ, high-redshift follow-ups are more available than low-mass ones. We will continue to factor in the total observational cost of a follow-up program, which is obtained by summing over the product of cluster number and cost in each bin.

##### 5.2. Optimizing the Follow-up Strategy at a Given Observational Cost

Given limited telescope time for a follow-up program, we would like to find the strategy that maximizes the FoM. However, our optimization algorithm in Section 3.2 cannot be applied directly; sampling a configuration at a given cost is not practical, since both the FoM and the cost depend on the configuration. We instead use a Monte Carlo approach: We sample a configuration and find its corresponding point on the cost–FoM plane. After sampling many configurations, we can find the boundary of these points and estimate the upper bound of the FoM at a given cost.

To generate these Monte Carlo points, we slightly modify the sampling algorithm in Section 3.2. At a given  $N_f$ , we sample  $\sim 10^5$  configurations and compute their corresponding cost and FoM. We then plot all these points on the cost–FoM plane and find the maximum of FoM at a given cost. To make the sampling more efficient, we modify the algorithm to maximize (FoM/ $\ln(\text{cost})$ ), which includes moderate dependence on cost. Since this objective function is not well justified, we

<sup>10</sup> We ignored the field-of-view limitations at low redshift when estimating this time scale, which is only used for order of magnitude estimates of the total telescope time required for a follow-up program.

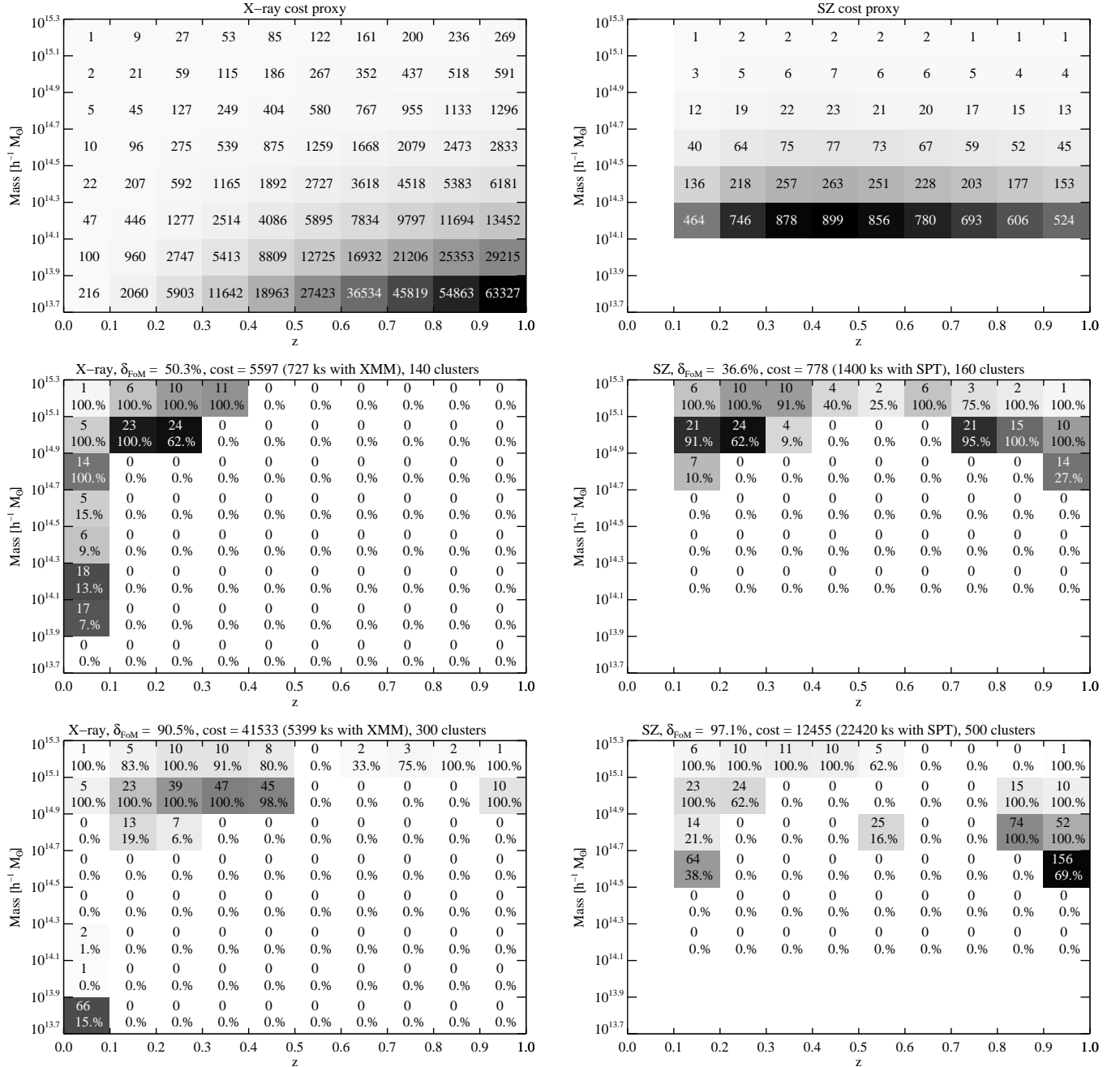


FIG. 5.— *Left*: X-ray follow-ups. *Right*: SZ follow-ups. *Top*: observational cost proxies, which are proportional to the required telescope time to observe a cluster and are normalized to the lowest-redshift and highest-mass bin available for each method. *Middle* and *bottom*: optimal follow-up strategies for small and large follow-up programs. We maximize the FoM at a given total cost and show both the number and percentage of follow-up targets in each bin. As can be seen, the configurations depend on the allowed cost. In general, X-ray follow-up programs favor low-redshift clusters first and extend to high-redshift as the allowed cost increases. On the other hand, SZ follow-ups include high mass clusters in a wide redshift range and extend toward low mass as the allowed cost increases.

only use it in the sampling. However, it turns out that the configuration maximizing (FoM/ $\ln(\text{cost})$ ) at a given  $N_f$  coincides with the boundary of the FoM at a given cost. We thus empirically propose that one can maximize (FoM/ $\ln(\text{cost})$ ) at a given  $N_f$  to design follow-ups.

The middle panels of Figure 5 show two examples of small follow-up programs involving about 150 clusters; both are the optimal strategies at a given cost. We present both the number

and the percentage of follow-ups in each bin. Comparing Figure 5 to Figure 2, we can see the impact of observational cost on designing follow-up strategies. For X-ray, as expected, the high-redshift and low-mass clusters are down-weighted because of their high cost; instead, clusters at low redshift are chosen. For SZ, due to its almost redshift-independent cost, massive clusters with a wide redshift range are preferred.

The bottom panels of Figure 5 present two examples of



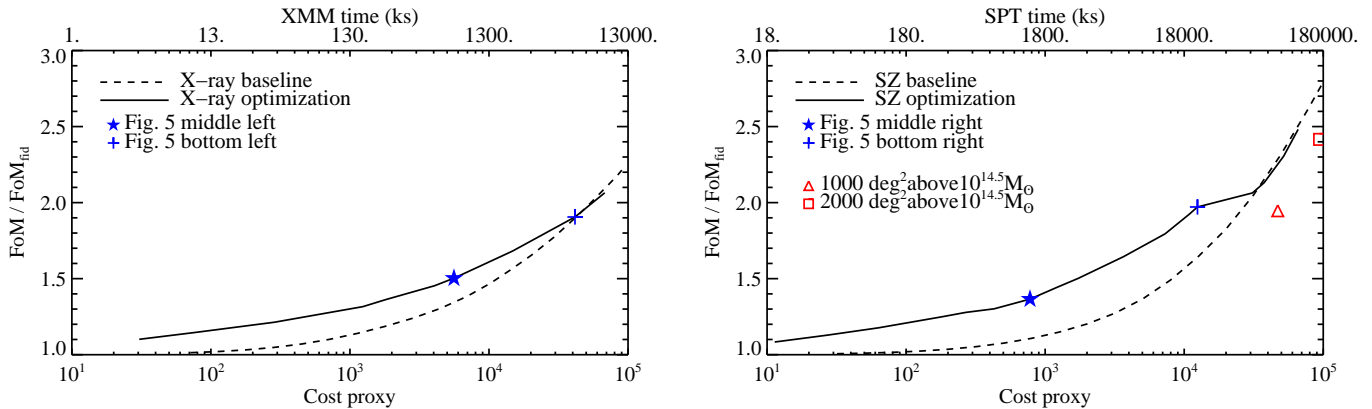


FIG. 6.— Improvement in the FoM as a function of observational cost. *Left*: X-ray follow-ups. *Right*: SZ follow-ups. The lower  $x$ -axes correspond to the cost proxies presented in Figure 5, while the upper  $x$ -axes correspond to the observational time for two specific instruments (see the text). The dashed curves correspond to evenly selected follow-ups with cost below 200, while the solid curve corresponds to optimal follow-up selections at each given cost. Both optimized curves show changes of slopes near the stars and crosses we marked, reflecting the changes of follow-up strategies. For small follow-up programs, optimal follow-up strategies can reduce the cost by up to an order of magnitude for a given FoM value. On the other hand, for large follow-up programs, optimizing with respect to cost is not essential. In the right panel, we also mark two points relevant to the SPT survey: 1000  $\text{deg}^2$  (triangle) and 2000  $\text{deg}^2$  (square), assuming a constant mass threshold  $10^{14.5} h^{-1} M_{\odot}$ .

large follow-up programs, both of which almost double the FoM. As the allowed cost increases, follow-up strategies change. These optimal configurations now extend toward the high-redshift and low-mass corners, as in the cases in Figure 2. For X-ray, the follow-ups include a wider range of mass and redshift. For SZ, less-massive clusters are included, and the configuration still favors a wide range in redshift.

These follow-up strategies are related to our assumptions that the observable–mass distribution depends on mass and redshift via power laws. To constrain power laws, sampling a range of mass and redshift is the most effective. We emphasize that these follow-up strategies are targeting dark energy constraints alone and do not comprehensively consider cluster science. In reality, skipping follow-ups in some bins may be risky for cluster science. In addition, we will need some follow-ups in every mass and redshift bin to test our power-law assumptions. After the power-law assumptions are justified, we can more confidently use our follow-up strategies to improve dark energy constraints. We also emphasize that a single instrument is assumed for the follow-up observations. For SZ, however, clusters of different redshift ranges are likely to be observed with different instruments with different normalizations in cost. These complications will be instrument specific and will change the optimization.

Figure 6 shows the FoM improvement due to optimization as a function of cost for both X-ray (left panel) and SZ (right panel) follow-ups. The lower  $x$ -axes correspond to the cost proxies discussed in Section 5.1, while the upper  $x$ -axes correspond to the telescope time specific to *XMM* and SPT. We compare the optimal cases (solid curves) with the baseline cases (dashed curves). The baseline cases correspond to equal number of follow-ups in all mass and redshift bins with cost less than 200. The importance of optimizing follow-up strategies is abundantly clear: to achieve a specified FoM, our optimal strategies can reduce the required telescope time by about an order of magnitude for small follow-up programs.

In Figure 6, the optimal cases for X-ray and SZ show different features. The stars and crosses mark the examples we have shown in Figure 5. As can be seen, for X-ray, as the allowed cost increases, the FoM increases less rapidly than SZ. Both curves show slope changes, which are caused by the changes

in configurations, as we discuss below.

For X-ray, when the allowed cost is below  $10^4$ , the most effective strategy is to tighten the constraints on the observable–mass distribution in low-redshift bins (as shown in the middle left panel in Figure 5). When the allowed cost is high enough, the follow-ups can afford to constrain both low and high redshift bins (as shown in the bottom left panel). Since constraining two extreme redshift regimes gives much better constraints on the evolution, the slope of the FoM increases. Nevertheless, this slope increase is very close to the point where the optimal case approaches the baseline case. With such a large allocation of telescope time, optimization is no longer essential, and the uniform sampling can achieve the same FoM.

For SZ, two obvious slope changes can be seen. The first one occurs near the cost of 1000. Below this cost, only massive clusters are chosen (as shown in the middle right panel of Figure 5). Above this cost, less-massive clusters become affordable (as shown in the bottom right panel), and the mass dependence of the observable–mass distribution is better constrained, leading to the slope increase of the FoM. The second change occurs near the cost of  $10^4$ , where the slope suddenly drops and the optimal case approaches the baseline case. At this point, we exhaust the information from the two redshift ends, and sampling the middle regime cannot make significant improvement. The lack of further improvement leads to the decrease of slope, and optimization is no longer essential when this amount of telescope time is available.

Comparing X-ray and SZ, we can view the design of cost-effective follow-up strategies as a trade-off between constraining mass dependence and constraining redshift evolution of the observable–mass distribution. When the cost is more sensitive to redshift than mass, as in the case of X-ray, one should prioritize the constraints on mass dependence regarding limited telescope time. On the other hand, when the cost is more sensitive to mass than redshift, as in the case of SZ, redshift evolution should be prioritized.

In the right panel of Figure 6, we add two points as references: the red triangle and the red square present the cases, respectively, of 1000 and 2000  $\text{deg}^2$  of SZ follow-ups; these assumptions are relevant for SPT. We assume a mass thresh-

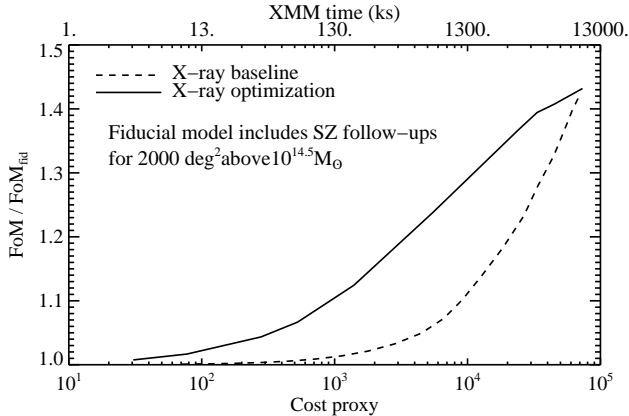


FIG. 7.— Improvement in the FoM as a function of observational cost from X-ray follow-ups in addition to 2000 deg<sup>2</sup> SZ observations above  $10^{14.5} h^{-1} M_{\odot}$ . These follow-up strategies all focus on low-redshift and low-mass clusters in order to provide complementary information to SZ follow-ups. We note that in this regime, the improvement in the FoM is less significant than previous cases because the fiducial FoM already includes substantial information from follow-ups.

old of  $10^{14.5} h^{-1} M_{\odot}$ , which roughly corresponds to the mass threshold of the ongoing SPT survey (L. Shaw & B. Benson 2009, private communication). However, here we assume that the follow-up mass measurements have a constant scatter and no systematic error. In reality, the SPT survey may not have the same precision in mass measurements for all clusters, and degradation due to inaccurate mass estimates is possible.

Finally, we study the complementarity between X-ray and SZ follow-ups. We assume that 2000 deg<sup>2</sup> of the survey field is followed up by SZ with a mass threshold of  $10^{14.5} h^{-1} M_{\odot}$ . We then optimize the X-ray follow-ups for clusters that are not observed by SZ. In Figure 7, we show the FoM improvement due to these additional X-ray follow-ups. The fiducial FoM corresponds to a DES-like survey with 2000 deg<sup>2</sup> SZ follow-ups, and the baseline case corresponds to evenly selected targets with cost below 200. To provide complementary information to SZ follow-ups, the optimal X-ray follow-up strategies would focus on low-redshift and low-mass clusters. We note that since the fiducial FoM already includes the information from SZ follow-ups, the improvement in the FoM is less significant than that in Figure 6.

In this calculation, we assume the SZ follow-up mass measurements have 20% scatter and no systematic error. This is an optimistic assumption for SPT; in reality, clusters observed by SPT may have larger scatter and more complicated sources of systematic error. Therefore, our calculation only represents a limiting case. On the other hand, our calculation assumes that X-ray and SZ follow-ups are not overlapping. In reality, some clusters will be observed with both methods. In principle, one can calculate the combined information from both X-ray and SZ follow-ups and optimize follow-up strategies by including these doubly followed-up clusters. However, since we assume very accurate mass inference for SZ clusters, X-ray observations will add little to it. In addition, computing the information from both follow-up methods will require modeling the full covariance between optical, X-ray, and SZ observables, which is beyond the scope of the current work.

## 6. DISCUSSION

In Section 4.1, we studied the impact of the correlation between different mass proxies. In principle, since the true mass is not observable,  $\rho$  cannot be directly measured. However, this correlation can be studied using consistency of scaling relations for different mass proxies. For example, Rykoff et al. (2008) studied the scaling relation of the mean X-ray luminosity and mean weak lensing mass for optically selected samples, which are binned by optical richness. They compared this scaling relation with the one derived from X-ray selected samples and found that the correlation between X-ray luminosity and optical richness is consistent with zero. Although these authors did not provide constraints on the correlation, they demonstrated an effective way to study it. In addition, Rozo et al. (2009a) used a similar analysis to obtain the constraints on the correlation between X-ray luminosity and mass for a given optical richness, finding  $\rho_{L_X, M|N} \geq 0.85$ .

This correlation can also be studied with simulations. For example, the results of Wechsler et al. (2006) imply a slight anti-correlation: at a given halo mass, halos with high concentration have lower richness on average. Cohn & White (2009) studied the joint SZ and optical cluster finding in simulations. They demonstrated that the cluster mass estimates from optical richness and SZ flux are positively correlated. Detailed comparisons for different mass proxies, however, will require further exploration (e.g., Stanek et al. 2009).

In Section 4.2, we studied the impact of the systematic error of follow-up mass measurements. Different follow-up methods have different sources of systematic error; here we compare several different mass proxies studied in the literature. Nagai et al. (2007) simulated the X-ray mass measurements and found that the total cluster mass derived from hydrostatic equilibrium is systematically lower than the true mass by about 5%–20% (also see, e.g., Rasia et al. 2006; Mahdavi et al. 2008). They also found that the deviation is less significant for relaxed systems and for the inner regions of the clusters. This underestimate can be attributed to the non-hydrostatic state of the intracluster medium that provides additional pressure support (e.g., Evrard 1990; Lau et al. 2009). On the other hand, they found that the estimate of the mass of the intracluster medium ( $M_{\text{gas}}$ ) is robust.

Vikhlinin et al. (2009a) used multiple X-ray indicators, including  $M_{\text{gas}}$ , the temperature  $T_X$ , and estimated total thermal energy  $Y_X = M_{\text{gas}} \times T_X$  to calibrate the cluster mass. These mass indicators have been shown by simulations to have a tight scaling relation with the total mass (e.g., Kravtsov et al. 2006). Vikhlinin et al. (2009a) also calibrated the total mass with low-redshift samples and cross-checked it with the weak lensing results. Therefore, X-ray clusters, when carefully calibrated, are likely to provide the most robust mass proxy and the most ideal method for follow-up observations.

On the other hand, SZ observations are still limited by statistics and have few observational studies on the scaling relation and the cluster profile (e.g., Mroczkowski et al. 2009; Bonamente et al. 2008). Their utility is thus yet to be fully demonstrated. In addition, Rudd & Nagai (2009) simulated the two-temperature model for clusters found that the non-equipartition of electrons and ions may lead to 5% underestimate of the mass derived from SZ. Nevertheless, simulations have shown that the scatter of the SZ mass proxy is small. If the systematic error can be well constrained, SZ follow-ups may become very influential given their statistical power in the near future.

Another possibility of follow-up observations is weak lensing mass measurements of individual clusters. Hoekstra

(2007) and Zhang et al. (2008) compared the mass measurements from weak lensing and X-ray, finding good agreement. However, weak lensing mass measurements usually have 20% uncertainties due to projection along the line of sight, and the current statistics are still low. In addition, detailed understanding of the photometric redshift properties of source galaxies is required to avoid systematic error in the recovered weak lensing mass (see e.g., Mandelbaum et al. 2008b).

Stacked weak lensing analysis has been used to measure the mean mass of the clusters for a given optical richness (e.g., Johnston et al. 2007; Mandelbaum et al. 2008a). This method does not suffer from projection effects caused by uncorrelated structure and allows one to estimate the mass of low-mass clusters, for which individual weak lensing cannot be detected. However, the stacked analysis cannot provide the variance of mass, which, as we have shown, contains important information. If the variance of mass can be determined using this method in the future (for example, by resampling), the constraining power of this method will be improved.

Finally, we note that one caveat of our results is the assumption that the optical richness–mass distribution is well described by a log-normal distribution and the scaling and scatter follow power laws. The validity of these assumptions will need to be tested explicitly with both simulations and observations.

## 7. CONCLUSIONS

We studied the impacts of follow-up observations—more precise measurements of cluster mass—on the constraining power of large optical cluster surveys. Considering the self-calibrated cluster abundance data from the DES, we demonstrated that the dark energy FoM can be significantly improved. Our primary findings are

1. Optimal target-selection strategies are essential for maximizing the power of modestly sized follow-up programs. For instance, 100 optimally selected follow-ups can improve the FoM of a DES-like survey by up to 76.4%, which is compared to a 40.3% improvement due to evenly selected follow-ups. Random sub-sampling of the cluster catalog is even less effective. Generally speaking, one should always follow up low-redshift clusters first, and then extend to the higher-redshift and lower-mass regime (Sections 3.1 and 3.2).
2. The scatter of the follow-up mass proxy and the covariance between the optical richness and the follow-up mass proxy have only modest effects on the FoM, provided that the follow-up mass proxy has sufficiently small scatter. On the other hand, although lowering the scatter of optical richness does not change the baseline

self-calibration results, it will significantly enhance the efficacy of follow-ups (Section 4.1).

3. Systematic error in follow-up mass measurements should be controlled at the 5% level to avoid severe degradation. In addition, if only the mean of cluster mass is measured, the systematic error of follow-up mass proxy will be degenerate with the systematic error of optical richness; measuring the variance of cluster mass can break this degeneracy (Section 4.2).
4. We explored observational issues to propose more practical X-ray and SZ follow-up programs. The observational costs of X-ray and SZ are, respectively, sensitive to redshift and mass, which in turn leads to different follow-up strategies. To achieve 50% improvement in the FoM, the most cost-effective follow-up strategy involves approximately 200 low-redshift X-ray clusters or massive SZ clusters. In general, our optimal strategies can reduce the observational cost required to achieve given dark energy constraints by up to an order of magnitude (Section 5).

A follow-up mass tracer that has systematic error understood at the 5% level will substantially benefit optical cluster surveys. On the other hand, reducing the scatter of optical mass tracer will significantly improve the efficacy of optically selected follow-ups. Current observational resources allow a few hundred low-redshift X-ray clusters, and in the near future hundreds or thousands of SZ clusters will become available. Therefore, detailed follow-up studies of a small but optimally-selected cluster sub-sample have the potential to be a powerful complement to current and imminent cluster surveys.

We thank Adam Mantz, Evan Million, Dan Marrone, and Brad Benson for help with estimating the observational cost of X-ray and SZ follow-ups, and Eli Rykoff for help with IDL routines. We also thank Michael Busha, Gus Evrard, Dragan Huterer, David Rapetti, and Laurie Shaw for helpful suggestions. We are grateful to the anonymous referee for helpful comments. We are also grateful for the support and hospitality of both CCAPP and KIPAC during collaboration visits. H.W. and R.H.W. were supported in part by the U.S. Department of Energy under contract number DE-AC02-76SF00515. H.W. received additional support from McMicking and Gabilan Stanford Graduate Fellowships. R.H.W. received support from a Terman Fellowship from Stanford University. E.R. is supported by the Center for Cosmology and Astroparticle Physics at the Ohio State University and by NSF grant AST 0707985.

## REFERENCES

- Albrecht, A. et al. 2006, arXiv:astro-ph/0609591  
 Böhringer, H. et al. 2004, *A&A*, 425, 367  
 Bonamente, M., Joy, M., LaRoque, S. J., Carlstrom, J. E., Nagai, D., & Marrone, D. P. 2008, *ApJ*, 675, 106  
 Carlstrom, J. E., Holder, G. P., & Reese, E. D. 2002, *ARA&A*, 40, 643  
 Cohn, J. D. & White, M. 2009, *MNRAS*, 393, 393  
 Cunha, C. 2009, *Phys. Rev. D*, 79, 063009  
 Cunha, C., Huterer, D., & Frieman, J. A. 2009, *Phys. Rev. D*, 80, 063532  
 Dunkley, J., Bucher, M., Ferreira, P. G., Moodley, K., & Skordis, C. 2005, *MNRAS*, 356, 925  
 Ebeling, H., Edge, A. C., Allen, S. W., Crawford, C. S., Fabian, A. C., & Huchra, J. P. 2000, *MNRAS*, 318, 333  
 Ebeling, H., Edge, A. C., Böhringer, H., Allen, S. W., Crawford, C. S., Fabian, A. C., Voges, W., & Huchra, J. P. 1998, *MNRAS*, 301, 881  
 Ebeling, H., Edge, A. C., & Henry, J. P. 2001, *ApJ*, 553, 668  
 Eisenhardt, P. R. M. et al. 2008, *ApJ*, 684, 905  
 Evrard, A. E. 1990, *ApJ*, 363, 349  
 Frieman, J. A., Huterer, D., Linder, E. V., & Turner, M. S. 2003, *Phys. Rev. D*, 67, 083505  
 Gladders, M. D., Yee, H. K. C., Majumdar, S., Barrientos, L. F., Hoekstra, H., Hall, P. B., & Infante, L. 2007, *ApJ*, 655, 128  
 Haiman, Z., Mohr, J. J., & Holder, G. P. 2001, *ApJ*, 553, 545  
 Henry, J. P., Evrard, A. E., Hoekstra, H., Babul, A., & Mahdavi, A. 2009, *ApJ*, 691, 1307  
 Hincks, A. D. et al. 2009, arXiv:0907.0461

- Hoekstra, H. 2007, *MNRAS*, 379, 317
- Holder, G. P., Haiman, Z., & Mohr, J. J. 2001, *ApJ*, 560, L111
- Holder, G. P., McCarthy, I. G., & Babul, A. 2007, *MNRAS*, 382, 1697
- Hu, W. 2003, *Phys. Rev. D*, 67, 081304
- Hu, W. & Cohn, J. D. 2006, *Phys. Rev. D*, 73, 067301
- Hu, W. & Kravtsov, A. V. 2003, *ApJ*, 584, 702
- Johnston, D. E. et al. 2007, arXiv:0709.1159
- Koester, B. P. et al. 2007, *ApJ*, 660, 239
- Komatsu, E. et al. 2009, *ApJS*, 180, 330
- Kravtsov, A. V., Vikhlinin, A., & Nagai, D. 2006, *ApJ*, 650, 128
- Lau, E. T., Kravtsov, A. V., & Nagai, D. 2009, *ApJ*, 705, 1129
- Levine, E. S., Schulz, A. E., & White, M. 2002, *ApJ*, 577, 569
- Lewis, A., Challinor, A., & Lasenby, A. 2000, *ApJ*, 538, 473
- Lima, M. & Hu, W. 2004, *Phys. Rev. D*, 70, 043504
- 2005, *Phys. Rev. D*, 72, 043006
- 2007, *Phys. Rev. D*, 76, 123013
- Mahdavi, A., Hoekstra, H., Babul, A., & Henry, J. P. 2008, *MNRAS*, 384, 1567
- Majumdar, S. & Mohr, J. J. 2003, *ApJ*, 585, 603
- 2004, *ApJ*, 613, 41
- Mandelbaum, R., Seljak, U., & Hirata, C. M. 2008a, *J. Cosmol. Astropart. Phys.*, 8, 6
- Mandelbaum, R. et al. 2008b, *MNRAS*, 386, 781
- Mantz, A., Allen, S. W., Ebeling, H., & Rapetti, D. 2008, *MNRAS*, 387, 1179
- Mroczkowski, T. et al. 2009, *ApJ*, 694, 1034
- Nagai, D., Vikhlinin, A., & Kravtsov, A. V. 2007, *ApJ*, 655, 98
- Parkinson, D., Blake, C., Kunz, M., Bassett, B. A., Nichol, R. C., & Glazebrook, K. 2007, *MNRAS*, 377, 185
- Parkinson, D., Kunz, M., Liddle, A. R., Bassett, B. A., Nichol, R. C., & Vardanyan, M. 2010, *MNRAS*, 401, 2169
- Postman, M., Lubin, L. M., Gunn, J. E., Oke, J. B., Hoessel, J. G., Schneider, D. P., & Christensen, J. A. 1996, *AJ*, 111, 615
- Press, W. H., Teukolsky, S. A., Vetterling, W. T., & Flannery, B. P. 2002, *Numerical recipes in C++ : the art of scientific computing* (Cambridge: University Press)
- Rasia, E. et al. 2006, *MNRAS*, 369, 2013
- Rozo, E., Wechsler, R. H., Koester, B. P., Evrard, A. E., & McKay, T. A. 2007a, astro-ph/0703574
- Rozo, E. et al. 2007b, astro-ph/0703571
- 2009a, *ApJ*, 699, 768
- 2009b, *ApJ*, 703, 601
- 2010, *ApJ*, 708, 645
- Rudd, D. H. & Nagai, D. 2009, *ApJ*, 701, L16
- Rykoff, E. S. et al. 2008, *MNRAS*, L58
- Sahlén, M. et al. 2009, *MNRAS*, 397, 577
- Shaw, L. D., Holder, G. P., & Bode, P. 2008, *ApJ*, 686, 206
- Sheth, R. K., Mo, H. J., & Tormen, G. 2001, *MNRAS*, 323, 1
- Stanek, R., Rasia, E., Evrard, A. E., Pearce, F., & Gazzola, L. 2009, arXiv:0910.1599
- Staniszewski, Z. et al. 2009, *ApJ*, 701, 32
- Tinker, J. L., Kravtsov, A. V., Klypin, A., Abazajian, K., Warren, M., Yepes, G., Gottlöber, S., & Holz, D. E. 2008, *ApJ*, 688, 709
- Tinker, J. L., Robertson, B. E., Kravtsov, A. V., Klypin, A., Warren, M. S., Yepes, G., & Gottlöber, S. 2010, arXiv:1001.3162
- Vikhlinin, A., McNamara, B. R., Forman, W., Jones, C., Quintana, H., & Hornstrup, A. 1998, *ApJ*, 502, 558
- Vikhlinin, A. et al. 2009a, *ApJ*, 692, 1033
- 2009b, *ApJ*, 692, 1060
- Wang, L. & Steinhardt, P. J. 1998, *ApJ*, 508, 483
- Wang, Y. 2008, *Phys. Rev. D*, 77, 123525
- Wechsler, R. H., Zentner, A. R., Bullock, J. S., Kravtsov, A. V., & Allgood, B. 2006, *ApJ*, 652, 71
- Wittman, D., Dell'Antonio, I. P., Hughes, J. P., Margoniner, V. E., Tyson, J. A., Cohen, J. G., & Norman, D. 2006, *ApJ*, 643, 128
- Wittman, D., Tyson, J. A., Margoniner, V. E., Cohen, J. G., & Dell'Antonio, I. P. 2001, *ApJ*, 557, L89
- Wu, H.-Y., Rozo, E., & Wechsler, R. H. 2008, *ApJ*, 688, 729
- Zhang, Y.-Y., Finoguenov, A., Böhringer, H., Kneib, J.-P., Smith, G. P., Kneissl, R., Okabe, N., & Dahle, H. 2008, *A&A*, 482, 451